

Experimental study of a CFD validation test case for turbulent separated flows

Owen Williams ^{*}, Madeline Samuell [†], Sage Sarwas [†], Matthew Robbins [†] and Antonino Ferrante [‡],
William E. Boeing Department of Aeronautics and Astronautics, University of Washington, Seattle, WA 98195, U.S.A.

An experimental and computational investigation of a new turbulent separated flow simulation validation test case at subsonic flow conditions is presented. Through close collaboration with Boeing, a three-dimensional tapered hump or “speed bump” geometry, relevant to a range of aerodynamic applications and central to an integrated testing/CFD campaign to improve turbulent RANS modeling is proposed. This study focuses on an examination of the flow over this geometry, as well as surveys of inflow boundary conditions, allowing the formalization of the domain, geometry and inflow length for corresponding CFD simulations. The analytically-defined geometric shape is tapered at the sides to minimize adverse side-wall flow interactions present in several previous bump experiments. Surface pressure and flow visualizations indicate the presence of moderate three-dimensionality at the centerline of the model but also a regime of Reynolds number independence, which is a desirable property for a validation test case. In contrast, while pressure coefficients computed from RANS simulations have similar magnitude to the experimental results, they fail to capture the Reynolds number insensitivity and profile inflection near reattachment that is observed in the experiments. These results suggest that the chosen geometry provides a strongly separated flow that is a challenging test for current RANS simulation capabilities.

I. Nomenclature

u	= streamwise velocity
U	= mean streamwise velocity
x	= streamwise coordinate
y	= spanwise coordinate
z	= wall-normal coordinate
p	= pressure
δ	= distance from wall where the velocity reaches $0.99U_\infty$
δ^*	= displacement thickness
θ	= momentum thickness
U_∞	= freestream velocity
u_τ	= friction velocity, $= \sqrt{\tau_w/\rho}$
Re_θ	= momentum thickness Reynolds number, $= \rho U_\infty \theta / \mu$
Re_τ	= friction Reynolds number, $= u_\tau \delta / \nu$
Re_x	= streamwise distance Reynolds number, $= U_\infty x / \nu$
C_f	= skin friction coefficient, $\tau_w / (0.5 \rho U_\infty^2)$
ΔU^+	= maximum deviation of boundary layer profile above log-law line in outer layer
C_p	= pressure coefficient
ν	= fluid kinematic viscosity
ρ	= fluid density
μ	= fluid dynamic viscosity
h	= bump height
H	= distance from top of splitter plate to tunnel ceiling
L	= wind tunnel width (36")

^{*}Assistant Research Professor, AIAA Member.

[†]Graduate Student.

[‡]Associate Professor, AIAA Senior Member

L_b	=	width of splitter plate (35.5")
x_0	=	parameter controlling streamwise extent of bump geometry
y_0	=	parameter controlling spanwise taper of bump toward side walls
h_0	=	parameter controlling bump height

Subscripts

∞	=	freestream conditions
tr	=	conditions at the trip

Superscripts

$+$	=	normalized using inner coordinates (u_τ and v/u_τ)
-----	---	--

II. Introduction

CFD is a critical element of the design process of modern, aerodynamically efficient airplanes and vehicles. Its capabilities have advanced significantly in both accuracy and complexity in recent years, with considerable progress in both computing power and numerical algorithms now making it possible to accurately simulate entire aircraft under cruise conditions, leading to reductions in wind tunnel and flight test time, and thus reductions in risk and cost. However large gaps remain in our understanding and quantitative prediction of turbulent flow separation present in complex aircraft configurations (such as approach and landing). While RANS simulations have proven successful in flows with small regions of separation, these methods still have significant difficulty predicting the point of flow separation over aerodynamically smooth surfaces, especially in the presence of a pressure gradient, as is common for practical situations. Hybrid-RANS and wall-modeled LES simulations both show promise in this area, however detailed and versatile data with which to validate and test new models and numerical algorithms is lacking [1].

Development and validation of improved turbulence models that allow the accurate prediction of vehicle forces and moments as well as the locations of flow separation and reattachment will require a highly detailed and tightly integrated experimental and numerical test campaign to help turbulence modelers diagnose, develop and improve both RANS and scale-resolving turbulence methods. This was a critical need identified in the CFD Vision 2030 study report published in 2014 [1]. Some initial progress toward this goal, highlighting the use of the speed bump geometry within a larger CFD validation context, is discussed by Slotnick et al [2]. In this paper, we provide details on the first stage of a Boeing-University of Washington collaborative effort to further explore the speed bump flow characteristics and improve our understanding of turbulent separated flows, in an effort to improve future simulation capabilities.

A number of previous studies of turbulent separated flow have been conducted in recent decades. These include studies of separated boundary layer flow due to an imposed pressure gradient [2], two-dimensional bumps of a range of shapes [3, 4], axisymmetric hill-type geometries[5–7], axisymmetric aft body flows [8, 9] and backward facing ramps [10]. While extremely valuable, further advancement of CFD necessitates increasingly stringent data fidelity and detail, with a focus on uncertainty quantification and minimization [11]. Previous two-dimensional geometries suffer from side-wall and streamline-divergence effects that are not understood or controlled to the extent now required. In addition, the separation location in some studies is strongly controlled by the geometry. New validation tests must challenge CFD capabilities to predict not only the turbulent separated region and reattachment but also the separation point. The effects of flow confinement that are unavoidable in wind tunnel testing must also be incorporated into the definition of any simulation test case to ensure accurate comparison between simulations and experiments. In addition, measurement capabilities and our ability to characterize inflow and boundary conditions have advanced considerably in recent years, providing significantly greater detail than previously possible.

The following study aims to conduct high-quality experiments designed specifically for CFD validation as part of a broader experimental and numerical collaboration aiming to advance our understanding of turbulent separated flows. This work focusses on the definition of a new computationally amenable test geometry and an initial assessment of its flow separation. This information is then used to formalize a matching CFD test case. Reynolds number sensitivities and the challenge posed to current RANS simulation methods will be assessed. Critically, the quantification and minimization of experimental uncertainties is central to this effort, with significant focus on the characterization of the wind tunnel as well as upstream boundary conditions. Experimental results reveal approximate Reynolds number independence and a surface pressure inflection point near reattachment that two- and three-dimensional RANS simulations fail to capture,

suggesting that this geometry is a suitable test of current turbulence models.

III. Methods and apparatus

A. Selection of validation test geometry

The final validation geometry was an elongated hill or “speed bump” configuration that is somewhat of an intermediary between previous two-dimensional hump and circular hill geometries [4–7]. This geometry was chosen to be amenable to simulation and serve a number of primary goals. First, it was tapered toward the side walls to avoid interactions with side-wall boundary layers. It also included two geometric planes of symmetry and one plane of flow symmetry, aiding in the quantification of bias errors or geometric imperfections of the as-manufactured experimental model. By choosing a geometry that was wider in the spanwise direction than the streamwise, it was also more wing-like in configuration and therefore more relevant to aircraft configurations. At the same time, the centerline flow would be detached and more approximately two-dimensional, with a three-dimensional attached flow toward the side-walls presenting a different type of challenge to CFD simulation.

Most critically, the geometry was chosen to provide a number of “control parameters” that would affect the extent of flow separation, beyond the expected variation with Reynolds number. The bump was mounted to a splitter plate upon which a fully developed turbulent boundary layer could be generated. The interaction of the boundary layer with the bump is a critical parameter for controlling separation, with the relative thicknesses of the boundary layer and bump height a parameter that can be tuned to be relevant to a range of applications.

While confinement effects in wind tunnels are not usually desired, it was acknowledged that the drive for larger Reynolds numbers would necessitate a larger model and that the removal of confinement-created pressure gradients cannot be fully avoided in any facility to the extent required of high-quality validation experiments. It was decided early in the design process that simulation of tunnel side walls and ceiling would be included in the final validation test case simulation definition. As a result, the splitter plate-to-ceiling distance, H , is an additional tunable parameter that can be used to control the extent of flow separation.

With all these considerations in mind, the proposed bump geometry follows the following function

$$z(x, y) = \frac{h_0}{2} e^{-\left(\frac{x}{x_0}\right)^2} \left[1 + \operatorname{erf}\left(\frac{\frac{L_b}{2} - 2y_0 - |y|}{y_0}\right) \right] \quad (1)$$

where x , y , z are the streamwise, spanwise and wall-normal directions, respectively. The length, L_b is the width of the splitter plate (35.5"). This width is only slightly different than the wind tunnel width, L , of 36". All results will be presented in terms of L which would be the width of corresponding simulations. For the current study, the control parameters were chosen to be $x_0 = 0.195L_b$, $y_0 = 0.06L_b$, $h_0 = 0.085L_b$, leading to a bump height, $h = 0.0838L$ and a maximum Reynolds number of $Re_L = 3.45 \times 10^6$. The bump geometry is plotted for streamwise and spanwise centerline planes in Figure 1.

B. Experimental apparatus

Experiments were conducted in the 3'x3' wind tunnel at the University of Washington. It is an open-return type with an 8 ft long test section and a velocity range of 10–60m/s, leading to a Reynolds number range of $0.69 \times 10^6 < Re_L < 3.6 \times 10^6$ based on the tunnel width, L , or $58 \times 10^3 < Re_h < 301 \times 10^3$ based on the bump height, h . It has a 200 HP, constant speed motor with pneumatically actuated variable pitch blades. The walls of the test section are plexiglass, giving excellent optical access. The inlet has a 9:1 contraction ratio, a honeycomb section near the inlet and a set of three screens. Temperature control is achieved through the manual operation of ceiling vent fans to the exterior of the building. The temperature was allowed to reach approximately steady state ahead of each test. At the commencement of this study the flow quality was surveyed, with excellent uniformity and freestream turbulence intensities of 0.2% or better across the velocity range.

A drawing of the splitter plate, including the locations of tripping devices and the boundary layer traverse, is shown in Figure 2 with units in inches. The middle section of the plate is interchangeable. For initial boundary layer studies, a flat plate was used in this section. This plate was replaced with the three-dimensional bump affixed to a 3/8" thick backing plate for later tests. For all of the following tests the upper surface of the splitter plate was positioned a distance $H/L = 0.5$ from the top wall of the tunnel however adjustment is possible for future study. The plate was mounted to a steel frame that was pinned to the tunnel walls. The splitter plate was constructed from MIC-6 Aluminum with a surface

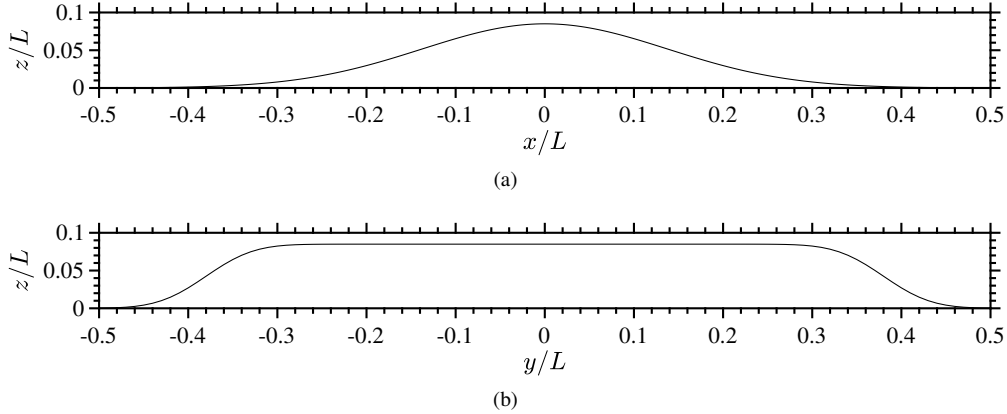


Fig. 1 Geometry of bump model in (a) streamwise and (b) spanwise directions relative to wind tunnel test section width, L .

roughness of less than $0.5\mu\text{m}$ and a maximum deviation from flat of 0.127mm (0.005"). The splitter plate was $L_b = 35.5"$ wide, allowing for clearances during assembly. The gap to the side walls either side of the plate was filled with adhesive-backed foam strips, forming an airtight seal.

The plate leading edge is 8 inches long with a 10:1 modified super-ellipse profile designed to have the greatest chance to maintain laminar or transitional flow over the leading edge and minimize any boundary layer initialization effects ahead of the trip [12]. It was 3D printed, sanded and painted. A tripping device was placed at the junction between the leading edge section and main plate (8" in the streamwise direction from the geometric leading edge). This location was a distance L from the top of the bump geometry. The turbulent boundary layer development length ahead of the boundary layer measurement location was 12.38" or $0.35L$. To ensure that the leading edge stagnation point could be placed at or above the geometric leading edge of the plate, a 12" trailing-edge flap could be adjusted using a single turnbuckle. The leading-edge incorporates two pairs of 1/32" static pressure taps on the top and bottom surfaces, a distance of 0.5" from the geometric leading edge and offset from the centerline by 5.75 inches. The pressure difference across these taps was used to set the flap such that the stagnation point lay above the geometric leading edge. For all following tests, the flap angle was set to 7°.

The freestream velocity was measured using the same Baratron 226a differential pressure transducer attached to the boundary layer pitot tube. This sensor has a range of 20 Torr and accuracy of 0.5% of full-scale. As this traversing mechanism could not remain in place while measuring surface pressures, as its wake would disturb the flow over the bump downstream, the freestream velocity was calibrated to the difference in static pressure between the inlet and entrance to the test section, as this measure of bulk tunnel velocity could be obtained without disturbing the flow. This static pressure difference was measured using an Omega PX653-10D5V pressure transducer with a range of 10" of water and accuracy of 0.5% of full-scale. This linear calibration was found to be highly repeatable. Atmospheric pressure was measured using a by a Digi-Sense Traceable Digital Barometer with a stated accuracy of 0.4kPa. Air temperature was measured using type-K thermocouple. Resulting uncertainty in freestream velocity was 1.1 m/s or 4.6% at 20m/s and 0.57m/s or 0.9% at 60m/s freestream velocity. Using propagation of uncertainty, the uncertainty in pressure coefficient was 9.7% at 20m/s and 2% at 60m/s.

The bump was constructed from epoxy and ATH powder by Steven Seim of CyberModelle. It was designed to be shimmed both vertically and horizontally to ensure alignment and close fit with the splitter plate. Six bolts hold the bump to a 3/8" aluminum backing plate that overlaps with the joints of the upstream and downstream splitter plate sections, providing alignment and rigidity. Speed tape covered the upstream and downstream seams between plate sections. To ensure pressure tap access, the underside of the bump was hollow with a maximum wall thickness of 0.5". The bump material thickness toward the edges of the bump was 3/8" such that the combination of bump and backing plate thicknesses would equal the splitter plate thickness of 0.75".

A total of 49 pressure taps were used, with nine on the splitter plate centerline upstream and downstream of the bump and the majority on the bump itself. All pressure taps were 1/32" diameter and drilled normal to the surface at all locations (locations summarized in Figure 9 and in the appendix). Along the top ridge of the bump these were drilled by CNC. At all other locations, a marker was mounted into the CNC chuck and gently touched to the surface of the bump to

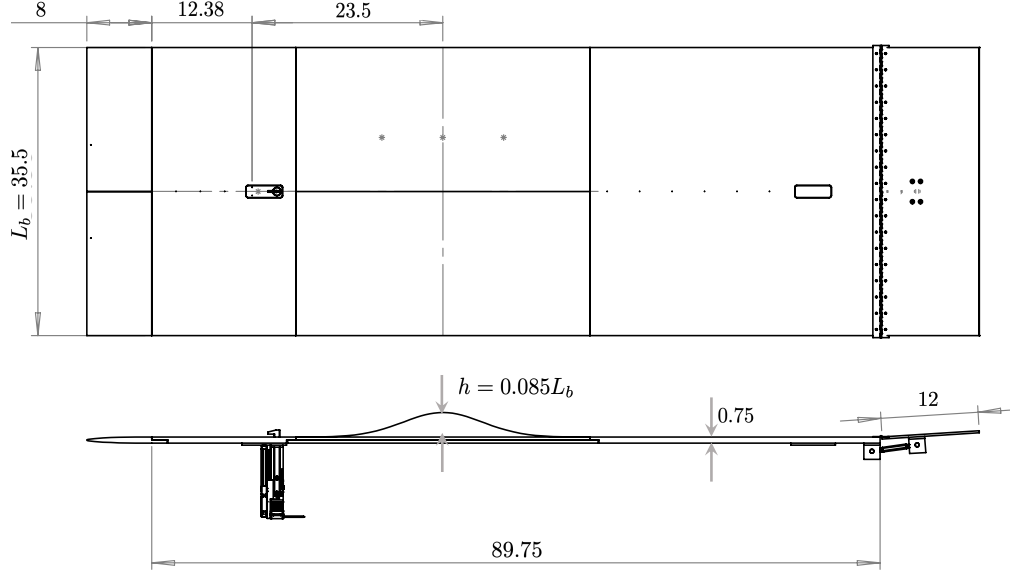


Fig. 2 Schematic of splitter plate, its three main sections, leading edge and trailing edge flap. A 0.25" gap is left between the plate and tunnel walls on each side. This is filled with neoprene rubber strips to prevent leakage around the edges of the plate. All dimensions in inches. The trips were located at the joint between the leading edge and first plate section.

indicate tap locations. A series of jigs, conforming to bump geometry at each tap location were then cut such that their edge could be used as an indicator of normalcy. Each tap was then carefully drilled by hand. To attach pressure tubing, a blind 1/16" hole was also drilled on underside of each pressure tap, co-linear to the primary 1/32" tap. A 1/16" OD stainless steel tube was then potted into each of these holes using epoxy. Plastic tube of 1/16" ID was affixed to each of these taps. Surface pressures were measured using a Baratron 226a differential pressure transducer with a range of 20 Torr and accuracy of 0.5% of full-scale. Each tap was selected sequentially using a Scannivalve solenoid for which 48 taps was the maximum. Tap one, located at $x/L = -0.8299$, was chosen as the reference pressure. It is hereafter designated as the reference pressure location when comparing with simulation datasets.

C. Boundary layer measurement

The splitter plate boundary layer mean velocity profile was measured $x/L = 0.35$ downstream from a series of tripping devices using a pitot tube and traversing mechanism. The traverse was mounted to a removable insert from the underside of the plate, with the pitot probe holder sliding up through a low friction PTFE slot. Wall-normal position of the probe was controlled by a Velmex UniSlide lead screw, driven by a LIN Engineering 417 stepper motor. To ensure very high accuracy, a Heidenhain SlimLine LS477 linear encoder with a step resolution of $0.5\mu\text{m}$ was mounted to the slide. Qualification tests indicated a maximum positional error of $\pm 0.58\mu\text{m}$ over the full slide length.

The closest probe position to the wall, z_0 was determined using calibrated macro-photography. A high-resolution Nikon DSLR camera was used for this purpose. The diameter of the probe and of its reflection on traverse mounting insert were used to determine the probe's position. Assuming these reference lengths were measured to within ± 1 pixel then the initial wall-normal position of the pitot probe is accurate to within $\pm 25\mu\text{m}$. Due to the thinness of the boundary layer a small pitot probe was required to achieve sufficient resolution. For the data included in this report, the probe diameter was 0.02" or 0.508mm. The static pressure was measured with two static taps machined into the traverse insert either side of the pitot tube. Pitot pressure was measured using a Baratron 226a differential pressure transducer with a range of 20 Torr and accuracy of 0.5% of full-scale.

D. Surface flow visualization

Surface flow patterns over the bump were visualized using a slurry of a kerosene, clay and Day-Glo powder which was painted over the model prior to tunnel startup. Once the tunnel was started, the clay moved to follow

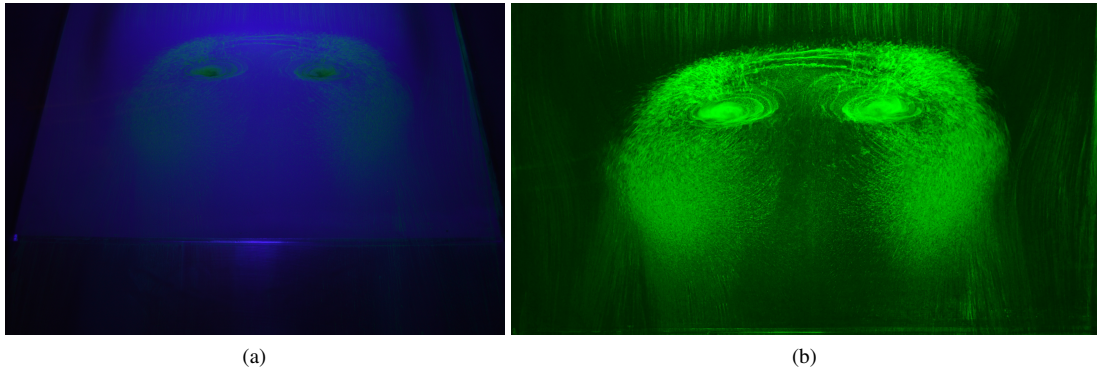


Fig. 3 (a) Raw surface visualization image with limited contrast and keystone perspective due to angle of viewing from the downstream direction. (b) Processed image. Flow is from top to bottom.

surface streamlines while the kerosene evaporated. Once evaporated, the tunnel was stopped and the surface patterns photographed. The surface was illuminated using an ultraviolet light, causing the mixture to fluoresce.

Images were acquired from the downstream side of the bump, looking at an upstream angle toward the separated region. The resulting images had a moderate keystone effect due to the perspective of the camera. An example of a raw image can be seen in Figure 3a. Note that, despite the fluorescent powder, the surface features remain difficult to discern in the raw image.

These raw images underwent a series of processing steps to remove the camera perspective and enhance the flow features. The keystone effect was removed using Photoshop, resulting in a bump image with sides parallel to the edges of the image and a constant spatial calibration. The image was also cropped to remove any regions outboard or downstream of the bump. Surface features were then enhanced by removing red and blue coloring, and by adjusting the brightness and contrast. An example of the result can be seen in Figure 3b.

IV. Qualification of splitter plate and incoming boundary layer

The effect of tripping on the mean boundary layer profile upstream of the bump was evaluated through the measurement of mean streamwise velocity profiles. The goal was to determine a minimal trip which produced a turbulent boundary layer over the range of Reynolds numbers of interest. The inflow length of corresponding simulations could then be defined to match the properties of the experimental boundary layer at the location of measurement.

A range of trips were tested including three grades of adhesive backed sandpaper (1" wide strip, 240, 120 and 60-grit) and low-profile Velcro (0.5" wide strip). The Velcro was the largest trip size, with a height of approximately 1mm, or 13% of the resulting boundary layer thickness, δ , at the profile measurement location. The boundary layer was initially examined with the bump replaced by a flat plate section at 30 and 60m/s corresponding to Re_L of 1.8×10^6 and 3.6×10^6 , respectively. The tripping devices were placed at the junction between the leading edge and plate.

The resulting boundary layer properties are detailed in Table 1. All boundary layers were found to be turbulent, with the exception of the untripped, 30m/s case, which was still transitional. Momentum thickness Reynolds numbers varied between $700 < Re_\theta < 1900$ at 30m/s and $1900 < Re_\theta < 3200$ at 60m/s. The momentum thickness was calculated by assuming a linear slope of the integrand between the surface first measured location at z_{min}^+ . The boundary layer thickness, δ was found to be approximately 10-12 times smaller than the chosen bump height, h , for all tripped cases. This lengthscale ratio was desirable, as it is relevant to aircraft applications. The development length was between 37δ and 49δ for tripped cases.

The resulting turbulent mean velocity profiles are plotted in inner coordinates in Figure 4. The friction velocity, $u_\tau = \sqrt{\tau_w / \rho}$, was determined using the Clauser chart method [13], fitting a portion of the mean velocity profile to the log-law with an assumed $\kappa = 0.421$ and intercept $B = 5.6$ [14].

Little variation was seen between the tripped cases at each flow velocity, with inner-scaling accounting for almost all deviations, despite the changes in trip size. Only the untripped cases had considerably smaller Reynolds numbers than their peers at the same velocity. These results suggest that the thickness of the sandpaper backing (0.6mm) may have a

Config.	Trip	Size	U_∞ [m/s]	δ [mm]	h/δ	$C_f \times 10^3$	Re_9	Re_τ	$Re_L \times 10^{-6}$	ΔU^+	z_{min}^+	Sym.
No Bump	None	-	30	2.7	28.4	-	694	-	1.75	-	-	○
		-	60	4.8	16.1	3.62	1892	785	3.48	1.93	53.5	●
	Sandpaper	240-grit	30	7.5	10.4	3.74	1617	629	1.78	1.98	26.9	☆
			60	6.4	12.2	3.23	2712	971	3.46	2.71	58.5	★
		120-grit	30	7.8	9.9	3.80	1673	669	1.79	1.66	31.2	□
			60	7.5	10.3	31.4	3140	1128	3.46	2.71	57.7	■
		60-grit	30	8.4	9.3	3.64	1876	722	1.85	2.02	31.8	△
			60	7.7	10.1	3.21	3188	1170	3.45	2.33	50.7	▲
	Velcro	$\sim 1\text{mm}$	60	7.8	10.0	3.20	3155	1172	3.44	2.35	48.8	▼
With Bump	Sandpaper	240-grit	20	7.7	10.1	4.22	1162	499	1.29	1.23	23.4	◊
		30	7.2	10.8	3.76	1559	639	1.87	1.94	60.0	◆	
		60	6.5	12.0	3.27	2638	967	3.39	2.57	67.4	◆	

Table 1 Test conditions for splitter plate boundary layer with a variety of tripping devices, with and without the bump present.

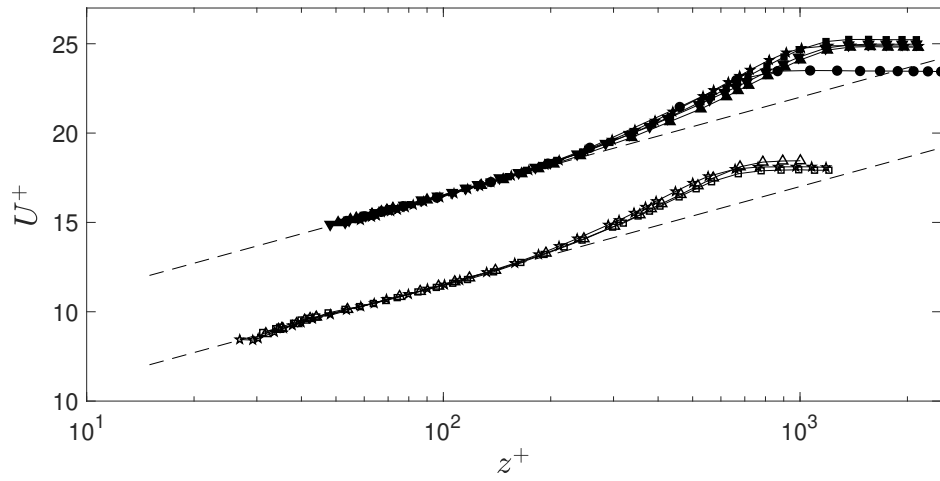


Fig. 4 Variation in inner-scaled mean velocity profile for different tripping devices with no bump present. Symbols as in Table 1. Turbulent cases only. Note shift in ordinate of 5 units for 60m/s cases (filled symbols). Dashed lines indicate log-law with $\kappa = 0.421$ and intercept $B = 5.6$.

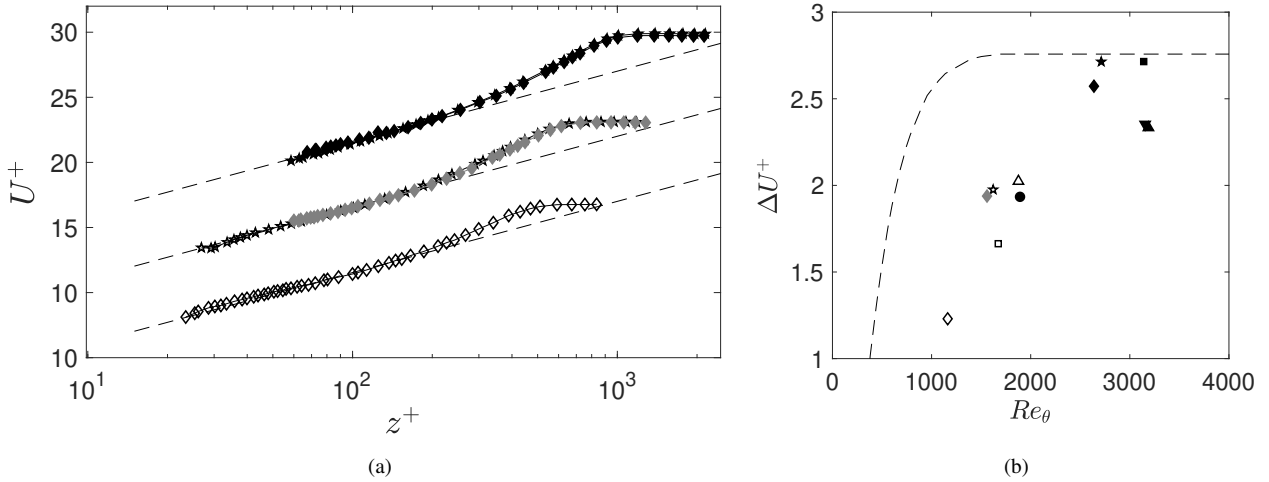


Fig. 5 (a) Comparison of inner-scaled mean velocity profiles, with and without the bump present. Note shift in ordinate. Dashed lines indicate log-law with $\kappa = 0.421$ and intercept $B = 5.6$. (b) Variation the maximum deviation of mean velocity profiles from the log-law in the outer layer, ΔU^+ . Results are compared with the correlation of Coles [15], indicated with a dashed line. Symbols as in Table 1.

more significant influence on the trip effectiveness than the grit roughness itself.

As the boundary layer was seen to be insensitive to the tested trips, the smallest, 240-grit sandpaper was chosen for subsequent testing with the bump present in the wind tunnel. A comparison between incoming boundary layers, with and without the bump, is shown in Figure 5a. The comparison for both velocities is excellent, indicating that the presence of the bump does not affect the incoming boundary layer at the location of the traverse. In anticipation of other measurements at 20m/s, the boundary layer was also surveyed at this velocity and found to be turbulent and consistent with previous results, but at a lower Reynolds number of $Re_\theta = 1160$.

As an extra test of boundary layer quality, the maximum deviation of the mean velocity profiles from the log-law in the outer layer, or

$$\Delta U^+ = \max \left[U - \frac{1}{\kappa} \ln \frac{zu_\tau}{v} - B \right] \quad \text{for } y/\delta > 0.2. \quad (2)$$

was examined. Otherwise known as the "wake size", Coles [15] demonstrated this measure to be indicative of both under- and over-tripping of boundary layers and hence a potential remaining influence of initial conditions. The variation in wake size with momentum thickness Reynolds number is plotted in Figure 5b for all turbulent cases. Also plotted is Coles' idealized correlation for the Reynolds number variation of wake size for correctly tripped boundary layers. The wake sizes at 60m/s compare favorably with expectations for all tripping devices. Cases at 20 and 30m/s appear to have wake components that are smaller than expected, however the wake size is more significantly influenced by small errors in the measurement of the first probe position at lower Reynolds numbers. As poor tripping or insufficient development length is known to often produce significantly greater deviations from Coles' correlation, the incoming boundary layer produced by the 240-grit trip was deemed to be satisfactory for further tests.

V. Corresponding Simulations

Two- and three-dimensional incompressible RANS simulations were conducted using commercial CFD software Star-CCM+ [16]. The Spalart-Allmaras turbulence model was used, with and without a curvature correction, which we denote as SA and SARC, respectively [17, 18]. The computational domain was configured to match the experimental geometry, including side walls and confinement.

Critically, experimental boundary layer results were used to standardize inflow conditions and boundary layer development lengths such that the simulated boundary layer achieved conditions (h/δ and Re_θ) that closely matched experiments at the location of boundary layer measurement ($x/L = -0.65$). The inflow length of $1.04L \pm 0.04$ upstream of the bump peak was estimated using the 2D zero pressure gradient, flat-plate verification test case standard for Re_θ

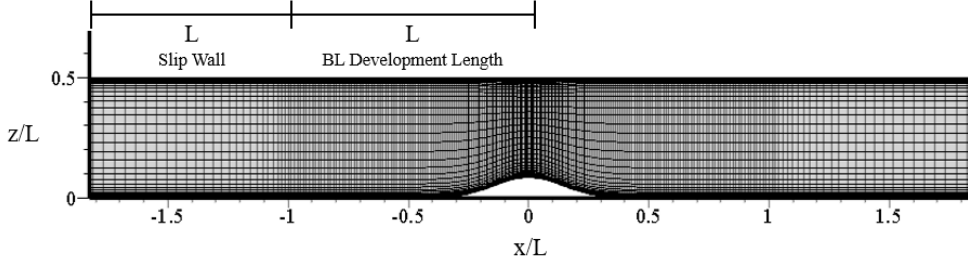


Fig. 6 Illustration of the two-dimensional, medium resolution body fitted mesh. The three-dimensional mesh was equivalent at the centerline.

variation with Re_x [19]. The slight variation is a result of performing this estimate over a number of boundary layer measurements over the range of flow velocities. For the purposes of this study, the inflow was standardized to $1L$, with resulting simulated boundary layer properties closely matching experiments.

A custom structured body-fitted gridding routine was created to ensure a smooth flow over the bump. A visualization of the medium resolution, two-dimensional mesh is shown in figure 6. The domain was $4L \times 0.5L$ with a no-slip boundary condition starting at a streamwise distance of L from the inlet plane on the top and bottom walls. A slip-wall boundary condition was applied at the top and bottom of the domain between the inlet plane and this location. A uniform velocity profile was applied at the inflow plane. A pressure outlet was used at the exit of the domain. Grid stretching was applied in the y -direction using a hyperbolic tangent stretching function. Stretching was also applied in the streamwise direction, using piecewise hyperbolic tangent and sine functions, which refined the grid over the bump and stretched the grid at the inflow and outflow.

The mesh for three-dimensional simulations was equivalent to the two-dimensional version on the centerline. A non-slip boundary condition was applied to the side-wall, starting a distance of L upstream of the bump peak. Grid stretching was applied in the z -direction using a hyperbolic tangent stretching function such that the resolution near the surface on the side-walls was equivalent to top and bottom walls.

A grid convergence study was conducted using the two-dimensional grid at the highest experimental Reynolds. Three grids of increasing refinement were employed. The coarse, medium and fine grids incorporated 130×60 , 260×80 and 390×120 grid points, respectively, leading to first grid points at $z_{min}^+ = 0.182, 0.141$, and 0.130 from the surface, at the boundary layer measurement location. Surface pressure and skin friction coefficient distributions for each grid are compared in Figure 7. The incoming boundary layer generated by each grid was found to closely match NASA's 2D zero pressure gradient flat plate verification test case [19]. As little difference is observed between the three grids, the medium resolution grid was selected for the remaining simulations at lower Reynolds number. The resolution of the three-dimensional mesh was equivalent to the two-dimensional mesh at the centerline. Similar stretching factors were employed in the spanwise direction resulting in a total number of grid points of $260 \times 80 \times 150$ in the x , y and z -directions respectively.

A series of six two-dimensional simulations were conducted, employing both SA and SARC models at three-Reynolds numbers in an effort to examine Reynolds number trends. Three-dimensional simulations were used to examine the influence of three-dimensionality of the flow at the model centerline and were conducted at the highest Reynolds number only. Resulting simulated boundary layer conditions and lengthscale ratios are provided in Table 2. These values were constant for a given Reynolds number, as expected, and did not vary between two and three-dimensional simulations or between SA and SARC models.

VI. Results

In an effort to understand the Reynolds number sensitivity of the chosen geometry and the ability of standard RANS models to simulate it, a series of china clay flow visualization and surface pressure measurements were conducted. Comparisons are made with 2D RANS simulations. A summary of test conditions and Reynolds numbers is presented in Table 2. Five velocities were investigated, from 20 to 60m/s corresponding to $Re_L = 1.3 - 3.45 \times 10^6$. Note the strong correspondence between experiments and simulations for important lengthscale ratios such as h/δ and h/θ due to the development length chosen for the simulation domain.

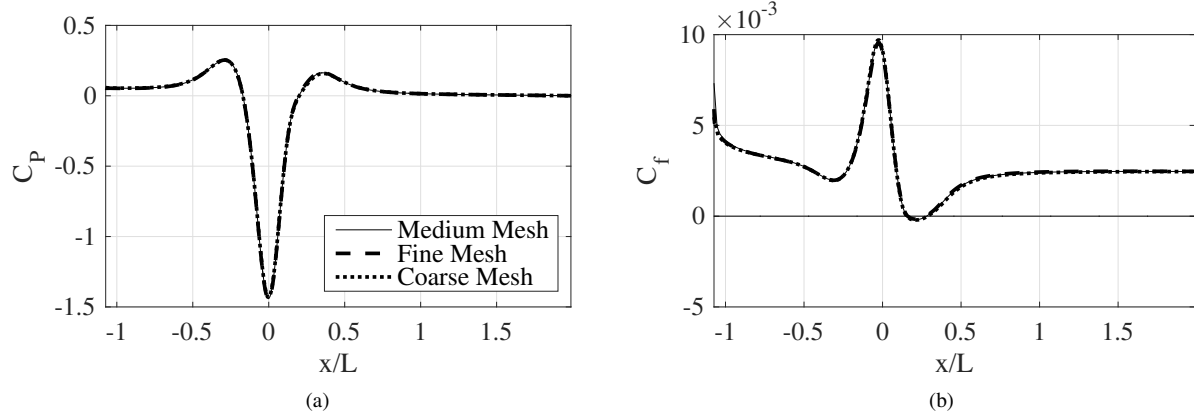


Fig. 7 Examination of grid convergence.

	Set Name	$Re_L (\times 10^{-6})$	$Re_h (\times 10^{-3})$	Ma	Re_θ	h/δ	h/θ
Exps.	20 m/s	1.32	112	0.07	1160	10.1	94.8
	30 m/s	1.87	159	0.10	1559	10.8	102
	40 m/s	2.46	209	0.13	-	-	-
	50 m/s	3.04	259	0.15	-	-	-
	60 m/s	3.41	290	0.17	2638	12.0	109
Sims.	20 m/s	1.17	99.5	-	1040	10.2	94.4
	40 m/s	2.34	199	-	1860	11.1	105.2
	60 m/s	3.51	299	-	2620	12.2	112.2

Table 2 Test conditions for experiments and 2D SA and SARC RANS simulations. Boundary layer properties in simulations are evaluated at the same distance downstream of the trip as in the experiments and were found to be identical for both models, as would be expected for attached flow.

A. Surface flow visualization

Multiple tests were conducted at all velocities faster than 30m/s using varying amounts of clay mixture. Two sample images for each velocity are shown in Figure 8. Axes have also been added to denote scale. The centerline of the bump in both streamwise and spanwise directions is indicated with red dashed lines.

The separated flow over the bump was found to concentrate the clay-kerosene mixture within the separated zone and often within two vortical structures. These surface vortices proved most challenging for this flow visualization technique and were sensitive to the amount of clay mixture used. The fluid was attracted to the vortex cores, where it would rotate, with droplets sometimes jumping away from the surface to be deposited elsewhere on the model. This sometimes blurs the separation and reattachment locations though they can still be discerned with reasonable accuracy. However, the thick film of kerosene in the vortex regions would also tend to run down the slope of the model. At higher velocities, the counterflow of the separated region would tend to hold the fluid in place, however this was not the case at the lowest velocities, resulting in a streamwise distortion of features within the separation bubble below 40m/s. It would take ten to fifteen minutes for the kerosene in the vortex cores to evaporate sufficiently so that the tunnel could be stopped and images acquired. For these reasons, flow visualization data was not obtained for a freestream velocity of 20m/s. It is also not possible to make firm conclusions regarding the movement of the surface vortex cores and changes to the size of the separated region with Reynolds number based on these visualizations.

Despite these challenges, valuable flow information can still be gained. Surface flow lines are clearly visible in the enhanced images, including a downstream saddle point on the centerline in most cases. This saddle point did not appear to move significantly with Reynolds number for the velocities tested here. Within uncertainty, the streamwise location of the separation line appears to be approximately constant for this range of velocities. These results hint at Reynolds number insensitivity that is corroborated by surface pressure measurements. In addition, these visualizations suggest the flow over this bump is at least partially three-dimensional over much of the span due to the chosen aspect ratio. The flow around the shoulders of the bump appear to be significant for $|y|/L > 0.25$.

B. Surface pressures

Surface pressures were measured at 49 locations along the splitter plate and over the bump for five streamwise velocities (20-60m/s). Test conditions are summarized in Table 2. The location and numbering of these pressure taps is summarized in Figure 9 and Table 3 in the appendix. Pressure taps were arranged in six spanwise planes that were symmetric either side of the centerline, allowing the estimation of any spanwise non-uniformity or bias errors, if present.

Variation in pressure by tap number is shown for all six cases in Figure 10. The first twenty taps correspond to the centerline of the tunnel, with subsequent taps in spanwise-symmetric pairs. While the pressures measured by pairs are not identical, no bias is observed toward either side of the bump, indicating flow symmetry.

The variation in pressure along the centerline is compared with simulations in Figure 11. All datasets (experimental and simulations) agree closely ahead of the bump, and downstream of the reattachment point, with differences confined largely to the separated zone, which is highlighted in Figure 12. Excellent agreement is observed between all experimental cases with freestream velocities faster than 40m/s, suggesting high Reynolds number independence of the separation zone. The experimental pressure profile deviates slightly downstream of the bump peak for the 30m/s case, while still following the higher Reynolds number profile closely.

The experimental 20m/s case shows the greatest departures from the other experimental data, with increasing pressure coefficient magnitudes immediately downstream of the bump peak and then relatively lower magnitude pressure coefficients downstream of $x/L = 0.1$. It is plausible that the flow is partially relaminarizing on the upstream slope of the bump at this Reynolds number. Further testing will be required to confirm this hypothesis.

All simulations are seen to compare poorly to the experiments in the separated region ($0.1 < x/L < 0.4$), despite closely following the experimental data in all other locations. In this region, simulated pressure coefficients are seen to be biased to more positive values for a given Reynolds number in all cases. In addition, the two-dimensional simulations are seen to vary continuously with Reynolds number, thus failing to predict the high Reynolds number independence observed experimentally. The Reynolds number trend observed in the simulations is also in the opposite direction to that observed experimentally at lower velocities. Differences between SA and SARC models are also greatest in the separated region, with SARC showing a slight improvement over the SA model. The difference between the two models, however, is relatively small.

Differences are observed between two and three-dimensional simulations, further reinforcing earlier assessments that three-dimensional effects are present at the model centerline. The minimum pressure at the bump peak is increased in magnitude in the two-dimensional simulations, consistent with the pressure relieving effects being present in the

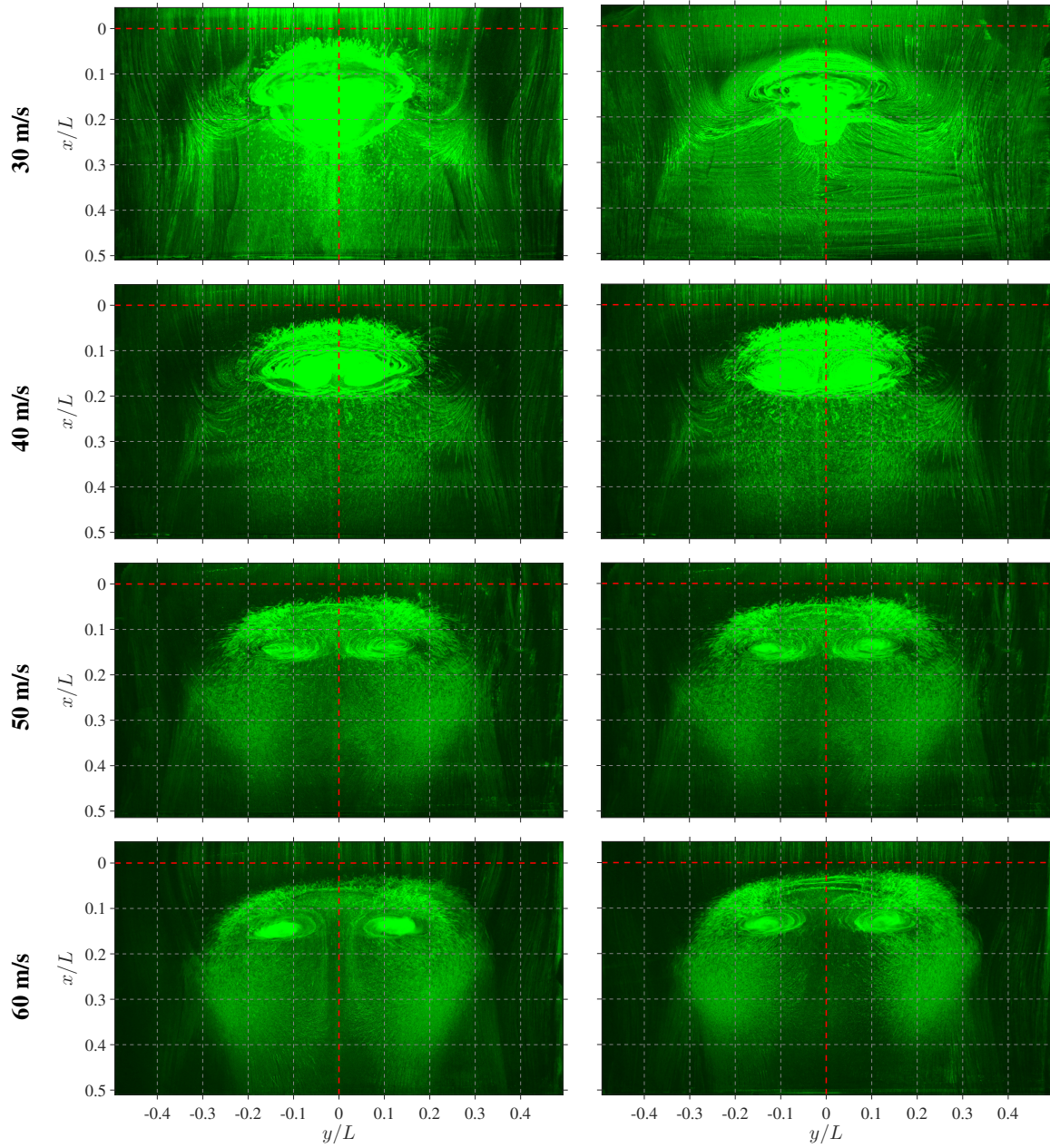


Fig. 8 China clay surface flow images for four tunnel velocities. Left and right columns are different realizations of the same test, using different quantities of clay. The centerline of the bump in both streamwise and spanwise directions is indicated with red dashed lines.

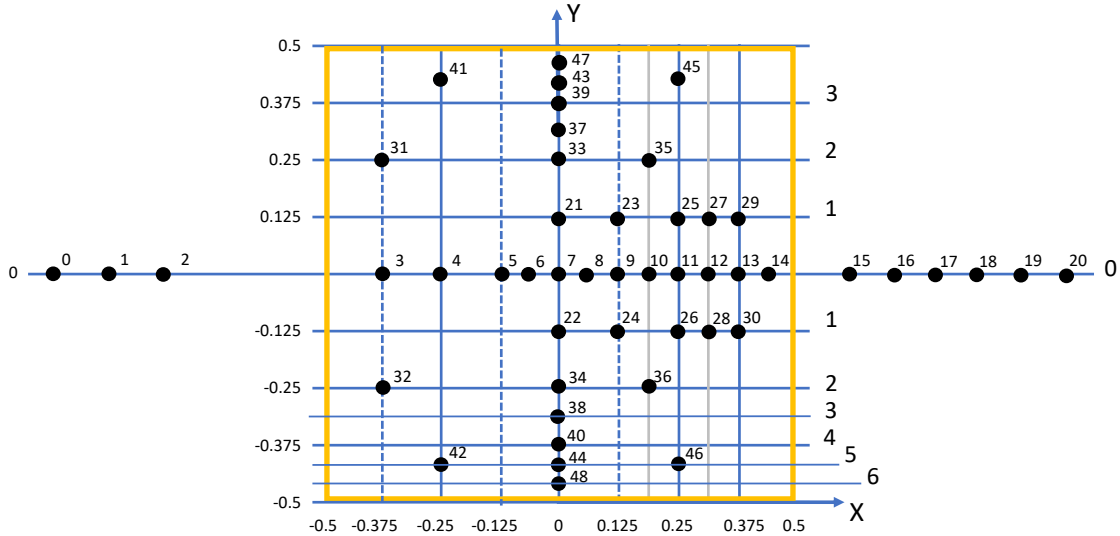


Fig. 9 Pressure tap numbering system and locations. Those taps outside the yellow box are positioned on the splitter plate centerline. All dimensions as a fraction of L_b . Plane number and tap locations locations summarized in Table 3 in appendix.

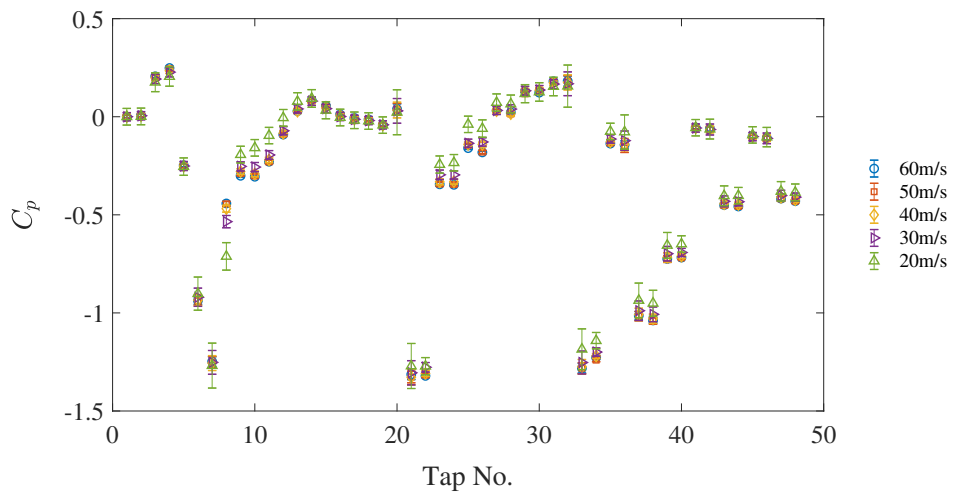


Fig. 10 Survey of all pressure coefficient data from current experiments. Tap numbers correspond to locations in Figure 9 and Table 3.

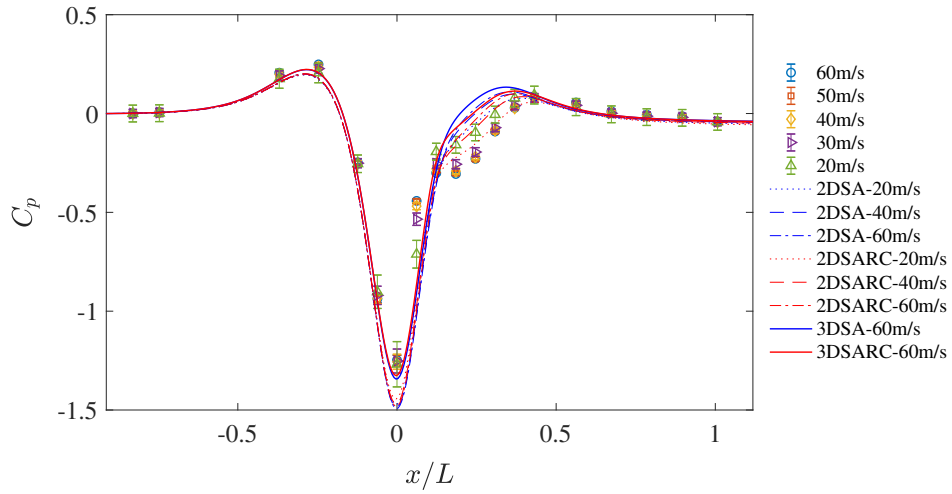


Fig. 11 Variation in pressure along the streamwise centerline.

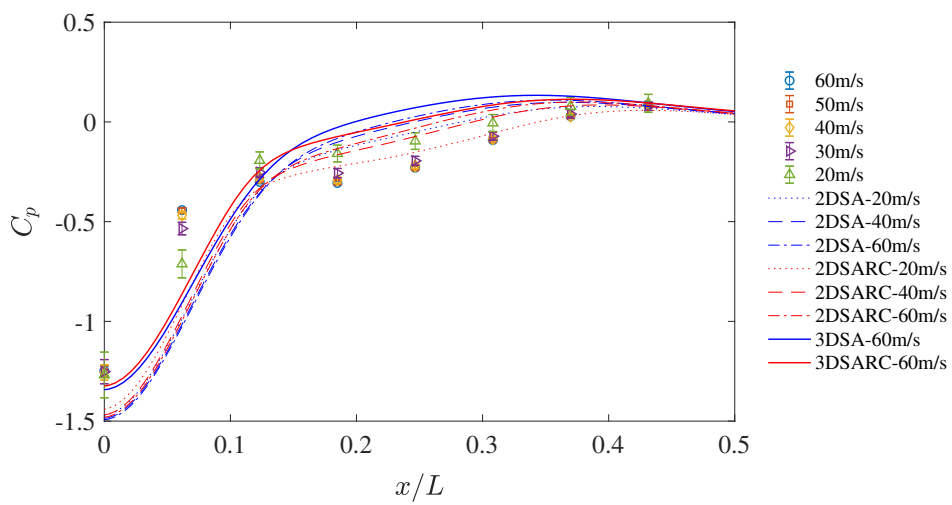


Fig. 12 Variation in pressure along the streamwise centerline, highlighting the separated region.

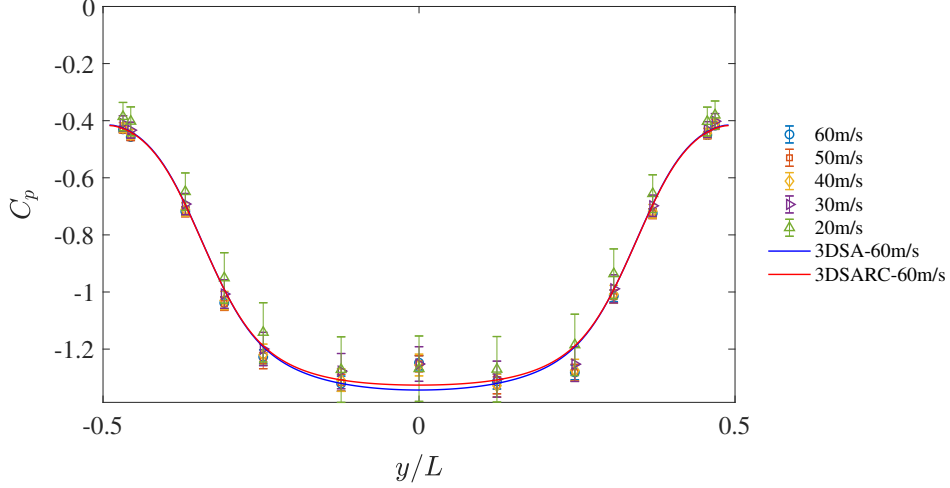


Fig. 13 Variation in pressure along the ridge of the bump ($x = 0$).

three-dimensional flow. More importantly, however, deviations between the simulations and experiments in the separated region are seen to be greatest for the three-dimensional simulations and both two- and three-dimensional simulations fail to capture the inflection observed in the experimental pressure profile between $0.1 < x/L < 0.2$.

The variation of pressure along the span of the bump ridge ($x = 0$) is shown in Figure 13. Experimental profiles tend toward a Reynolds number independent profile at high velocities, as with the streamwise profiles. Interestingly, the experimental pressure coefficients at the top center of the bump are very similar in all cases. At lower velocities, this pressure is relatively constant across the top of the bump before reducing in magnitude toward the shoulders. At higher Reynolds numbers, however, the magnitude of the pressure coefficient forms two shallow peaks either side of the centerline that are approximately 2.5% greater in magnitude than the centerline pressure. This feature was found to be highly repeatable but is not observed in the simulations for either SA or SARC turbulence models. These simulations closely followed the experimental results along the top of the bump and toward the shoulders in all other respects.

VII. Discussion and conclusions

This paper details the definition and initial investigation of a turbulent separated flow validation test case. An elongated hump or “speed bump” was selected to avoid side-wall interactions and to be applicable to wing-like geometries. It was mounted to a splitter plate which generated a fully developed turbulent boundary layer upstream. The properties of this boundary layer were examined, allowing the selection of a tripping device minimizing upstream influences and the formalization of the CFD test-case inflow to be $x/L = 1$ upstream of the bump peak.

Two surface vortices dominate the separated flow structure, with separated flow inboard of these vortices and three-dimensional attached flow further toward the side walls. Flow visualization and surface pressure results suggest that the separated flow downstream of the bump is Reynolds number invariant for $Re_L > 2.4 \times 10^6$, as is desirable for a validation test case. The flow visualizations are harder to interpret in this regard, with the location of the separation line and saddle points supporting this conclusion within uncertainty. Both measures also suggest some three-dimensional effects extend to the centerline of the bump.

The departure of the surface pressure profile at low velocities is thought likely to be due to partial relaminarization of the flow on the upstream face of the bump, however further tests are required to confirm this hypothesis. Interestingly, profiles of pressure across the spanwise ridge of the bump display a shallow double-peaked profile either side of the centerline at high Reynolds numbers. Capturing this feature could form the basis for discrimination of the quality of future turbulence models.

Two- and three-dimensional simulations were seen to have similar profile shape and magnitude to the the experiments outside the separated region. Within the separated region, however, both SA and SARC models displayed continual variation with Reynolds number and a profile shape that failed to capture an inflection point visible in the experiments. While the SARC model more closely matched the experimental results, the improvement was slight. Surprisingly, three-dimensional simulations deviated more greatly from the experiments at a given Reynolds number in this region,

further highlighting the challenge posed by this geometry.

The chosen validation test geometry meets all initial goals. Inflow lengths required for simulations to match experiments were found to be insensitive to Reynolds number but most importantly, the flow was found to be independent of Reynolds number for freestream velocities above 40m/s, with only moderate three-dimensionality to the centerline. In addition, a number of surface pressure profile features were identified that appear challenging for current turbulence model capabilities. With regions of attached, separated and recovering flow, this geometry is primed to advance NASA's CFD 2030 goals.

Appendix

Please refer to Table 3 for the locations of the surface pressure taps.

Acknowledgments

The support of Boeing Commercial Aircraft and their Flight Sciences Function Excellence group is gratefully acknowledged. Especially that of Jeffrey Slotnick and Philippe Spalart for their significant technical and administrative support for this effort.

The authors would also like to thank Eliot George and Dzung Tran for the invaluable assistance constructing the splitter plate and traverse apparatus. Members of the Kirsten Wind Tunnel are also acknowledged for their experience with the china clay formulation.

The manufacture of the bump test article was conducted by Steven Seim of CyberModelle, to whom we owe a debt of gratitude for his tireless effort.

References

- [1] Slotnick, J., Khodadoust, A., Alonso, J., Darmofal, D., Gropp, W., Lurie, E., and Marvriplis, D., "Vision 2030 CFD study: A path to revolutionary computational aerosciences," Tech. rep., NASA/CR-2014-218178, 2014.
- [2] Driver, D., "Reynolds shear stress measurements in a separated boundary layer flow," *AIAA-1991-1787, 22nd Fluid Dynamics, Plasma Dynamics and Lasers Conference, Honolulu, HI*, 1991.
- [3] Webste, D., DeGraaff, D., and Eaton, J., "Turbulence characteristics of a boundary layer over a swept bump," *Journal of Fluid Mechanics*, Vol. 323, 1996, pp. 1–22.
- [4] Greenblatt, D., Paschal, K., Schaeffler, N., Washburn, A., and Yao, C., "Separation control over a wall-mounted hump: A CFD validation test case," *AIAA Paper 2004-2219*, 2004.
- [5] Byun, G., and Simpson, R. L., "Structure of three-dimensional separated flow on an axisymmetric bump," *AIAA Journal*, Vol. 44, No. 5, 2006.
- [6] Bell, J., Heineck, J., Zillac, G., Mehta, R., and Long, K., "Surface and flow field measurements on the FAITH Hill Model," *AIAA-2012-0704*, 2012.
- [7] Husen, N., Woodiga, S., Liu, T., and Sullivan, J., "Global luminescent oil-film skin friction meter generalized to three-dimensional geometry and applied to FAITH Hill," *AIAA SciTech Forum*, 2014.
- [8] Bachalo, W., and Johnson, D., "Transonic turbulent boundary-layer separation generated on an axisymmetric flow model," *AIAA-1979-1479, AIAA 12th Fluid and Plasma Dynamics Conference, Williamsburg, VA*, 1979.
- [9] Disotell, K. J., and Rumsey, C. L., "Design of an Axisymmetric afterbody test case for CFD Validation," *AIAA 2017-3792*, 2017.
- [10] Simmons, D., Thomas, F., and Corke, T., "Benchmark smooth body flow separation experiments," *AIAA Aviation Forum*, 2017.
- [11] Oberkampf, W. L., and Smith, B. L., "Assessment Criteria for computational fluid dynamics validation benchmark experiments," *AIAA SciTech Forum*, 2014.
- [12] Hanson, R. E., Buckley, H. P., and Lavoie, P., "Aerodynamic optimization of the flat-plate leading edge for experimental studies of laminar and transitional boundary layers," *Experiments in Fluids*, Vol. 53, 2012, pp. 863–871.
- [13] Clauser, F. H., "Turbulent boundary layers in adverse pressure gradients," *Journal of Aerospace Sciences*, Vol. 21, 1954, pp. 91–108.

- [14] McKeon, B., Li, J., Jiang, W., Morrison, J., and Smits, A., “Further observations on the mean velocity distribution in fully developed pipe flow,” *Journal of Fluid Mechanics*, Vol. 501, 2004, pp. 135–147.
- [15] Coles, D., “The turbulent boundary layer in a compressible fluid,” Tech. rep., Report R-403-PR, The Rand Corporation, Santa Monica, California, 1962.
- [16] ANSYS Inc., “ANSYS CFD-Post,” Tech. rep., ANSYS Inc., 2017.
- [17] Spalart, P. R., and Allmaras, S. R., “A One-Equation Turbulence Model for Aerodynamic Flows,” *Recherche Aerospatiale*, Vol. 1, 1994, pp. 5–21.
- [18] Shur, M., Strelets, M., Travin, A., and Spalart, P., “Turbulence Modeling in rotating and curved channels: Assessing the Spalart-Shur Correction,” *AIAA Journal*, Vol. 38, No. 5, 2000, pp. 784–792.
- [19] “NASA’s 2D Zero Pressure Gradient Flat Plate Verification Case - Turbulence modelling resource,” , 2019. URL <https://turbmodels.larc.nasa.gov/flatplate.html>.

Tap No.	Plane	y/L_b	x/L_b	y/L	x/L	C_p ($Re_L = 3.6 \times 10^6, 60 - 2$)	C_p ($Re_L = 1.8 \times 10^6, 30 - 2$)
0	0	0.0000	-0.9261	0.0000	-0.9132	-	-
1		0.0000	-0.8415	0.0000	-0.8299	5.36E-03	4.32E-04
2		0.0000	-0.7570	0.0000	-0.7465	6.82E-03	1.08E-03
3		0.0000	-0.3750	0.0000	-0.3698	1.99E-01	1.86E-01
4		0.0000	-0.2500	0.0000	-0.2465	2.29E-01	2.13E-01
5		0.0000	-0.1250	0.0000	-0.1233	-2.50E-01	-2.61E-01
6		0.0000	-0.0625	0.0000	-0.0616	-9.07E-01	-9.19E-01
7		0.0000	0.0000	0.0000	0.0000	-1.20E+00	-1.26E+00
8		0.0000	0.0625	0.0000	0.0616	-4.25E-01	-5.55E-01
9		0.0000	0.1250	0.0000	0.1233	-3.10E-01	-2.68E-01
10		0.0000	0.1875	0.0000	0.1849	-3.16E-01	-2.72E-01
11		0.0000	0.2500	0.0000	0.2465	-2.41E-01	-2.13E-01
12		0.0000	0.3125	0.0000	0.3082	-1.09E-01	-8.59E-02
13		0.0000	0.3750	0.0000	0.3698	1.16E-02	2.23E-02
14		0.0000	0.4375	0.0000	0.4314	7.28E-02	6.97E-02
15		0.0000	0.5704	0.0000	0.5625	4.93E-02	3.93E-02
16		0.0000	0.6831	0.0000	0.6736	8.08E-03	-1.93E-03
17		0.0000	0.7958	0.0000	0.7847	-1.05E-02	-2.05E-02
18		0.0000	0.9085	0.0000	0.8958	-2.28E-02	-3.05E-02
19		0.0000	1.0211	0.0000	1.0069	-4.19E-02	-4.69E-02
20		0.0000	1.1338	0.0000	1.1181	-1.25E+00	-1.27E+00
21	1	0.1250	0.0000	0.1233	0.0000	-1.28E+00	-1.31E+00
22		-0.1250	0.0000	-0.1233	0.0000	-3.45E-01	-3.08E-01
23		0.1250	0.1250	0.1233	0.1233	-3.47E-01	-3.07E-01
24		-0.1250	0.1250	-0.1233	0.1233	-2.21E-01	-1.89E-01
25		0.1250	0.2500	0.1233	0.2465	-1.55E-01	-1.08E-01
26		-0.1250	0.2500	-0.1233	0.2465	-4.44E-02	-6.02E-02
27		0.1250	0.3125	0.1233	0.3082	1.68E-02	-1.36E-02
28		-0.1250	0.3125	-0.1233	0.3082	7.98E-02	6.18E-02
29		0.1250	0.3750	0.1233	0.3698	1.42E-01	1.45E-01
30		-0.1250	0.3750	-0.1233	0.3698	1.73E-01	1.64E-01
31	2	0.2500	-0.3750	0.2465	-0.3698	1.70E-01	1.61E-01
32		-0.2500	-0.3750	-0.2465	-0.3698	-1.23E+00	-1.23E+00
33		0.2500	0.0000	0.2465	0.0000	-1.20E+00	-1.19E+00
34		-0.2500	0.0000	-0.2465	0.0000	-1.60E-01	-1.65E-01
35		0.2500	0.1875	0.2465	0.1849	-1.52E-01	-1.37E-01
36		-0.2500	0.1875	-0.2465	0.1849	-9.80E-01	-9.79E-01
37	3	0.3125	0.0000	0.3082	0.0000	-1.02E+00	-1.01E+00
38		-0.3125	0.0000	-0.3082	0.0000	-7.12E-01	-6.98E-01
39	4	0.3750	0.0000	0.3698	0.0000	-7.03E-01	-6.90E-01
40		-0.3750	0.0000	-0.3698	0.0000	-6.42E-02	-6.88E-02
41	5	0.4625	-0.2500	0.4561	-0.2465	-6.88E-02	-7.17E-02
42		-0.4625	-0.2500	-0.4561	-0.2465	-4.50E-01	-4.38E-01
43		0.4625	0.0000	0.4561	0.0000	-4.50E-01	-4.33E-01
44		-0.4625	0.0000	-0.4561	0.0000	-1.21E-01	-1.21E-01
45		0.4625	0.2500	0.4561	0.2465	-1.23E-01	-1.27E-01
46		-0.4625	0.2500	-0.4561	0.2465	-4.22E-01	-4.14E-01
47	6	0.4750	0.0000	0.4684	0.0000	-4.23E-01	-4.11E-01
48		-0.4750	0.0000	-0.4684	0.0000	-2.99E-02	-3.36E-02

Table 3 Summary of pressure tap locations organized by spanwise plane number indicated in Fig. 9.